

Coupling a single spin to high-frequency motion

Federico Fedele,^{1,*} Federico Cerisola,^{2,1,*} Lea Bresque,³ Florian Vigneau,⁴ Juliette Monsel,⁵
Jorge Tabanera,⁶ Kushagra Aggarwal,⁴ Jonathan Dexter,⁴ Sofia Sevitz,⁷ Joe Dunlop,²
Alexia Auffeves,^{3,8} Juan Parrondo,⁶ Andras Palyi,^{9,10} Janet Anders,^{2,7} and Natalia Ares^{1,†}

¹*Dept. of Engineering Science, University of Oxford, Oxford OX1 3PJ, United Kingdom.*

²*Dept. of Physics and Astronomy, University of Exeter, Stocker Road, EX4 4QL, United Kingdom.*

³*Univ. Grenoble Alpes, CNRS, Grenoble INP, Institut Néel, 38000 Grenoble, France.*

⁴*Dept. of Materials, University of Oxford, Oxford OX1 3PH, United Kingdom.*

⁵*Dept. of Microtechnology and Nanoscience (MC2), Chalmers University of Technology, S-412 96 Göteborg, Sweden.*

⁶*Dept. of Structure of Matter, Thermal Physics and Electrodynamics and GISC, Universidad Complutense de Madrid, Pl. de las Ciencias 1. 28040 Madrid, Spain.*

⁷*Institute of Physics and Astronomy, University of Potsdam, 14476 Potsdam, Germany.*

⁸*MajuLab, National University of Singapore, 117543 Singapore.*

⁹*Dept. of Theoretical Physics, Budapest University of Technology and Economics, Műegyetem rkp. 3., H-1111 Budapest, Hungary.*

¹⁰*HUN-REN-BME Quantum Dynamics and Correlations Research Group, Műegyetem rkp. 3., H-1111 Budapest, Hungary*

Coupling a single spin to high-frequency mechanical motion is a fundamental bottleneck of applications such as quantum sensing [1, 2, 4, 7], intermediate and long-distance spin-spin coupling [3], and classical and quantum information processing [6]. Previous experiments have only shown single spin coupling to low-frequency mechanical resonators, such as diamond cantilevers [4, 15, 17, 20, 21]. High-frequency mechanical resonators, having the ability to access the quantum regime, open a range of possibilities when coupled to single spins, including readout and storage of quantum states. Here we report the first experimental demonstration of spin-mechanical coupling to a high-frequency resonator. We achieve this all-electrically on a fully suspended carbon nanotube device. A new mechanism gives rise to this coupling, which stems from spin-orbit coupling, and it is not mediated by strain [34]. We observe both resonant and off-resonant coupling as a shift and broadening of the electric dipole spin resonance (EDSR), respectively. We develop a complete theoretical model taking into account the tensor form of the coupling and non-linearity in the motion. Our results propel spin-mechanical platforms to an uncharted regime. The interaction we reveal provides the full toolbox for promising applications ranging from the demonstration of macroscopic superpositions [48], to the operation of fully quantum engines [42, 43, 45], to quantum simulators [8].

The ability to couple a single spin to mechanical motion emerges as a requirement for quantum technological applications [1–7]. Mechanical resonators can extend over macroscopic distances and exhibit large quality factors. This means that the coupling between spin and motion can be used to connect well-separated locations on chip and to store quantum information, enabling hybrid quantum networks [9]. Unlike most of the alternatives for intermediate and long-range spin-spin coupling, mechanical resonators can exhibit longitudinal parametric coupling to spins [15], enabling low power entangling operations [11] and fast quantum-non-demolition readout of the spin states [12]. Spin mechanical coupling is highly desired to enable teleportation and entanglement swapping of macroscopic states of motion [10].

Recent advances in magneto-mechanical sensing are also finding practical applications in biology and biomedicine [13, 14]. From a fundamental perspective, the coupling between spins and mechanics is key to the exploration of the quantum-to-classical transition. These

prospects have motivated extensive theoretical and experimental work to achieve coupling between single spins and mechanical resonators that can be operated in the quantum regime [16–18].

The interaction between single spins and mechanics has been demonstrated for a single NV spin-qubit probed by a magnetized AFM cantilever [4, 19], as well as in monolithic platforms, where single NV spin-qubits are embedded in cantilevers and semiconductor nanowires [15, 20–23], and with an InGaAs quantum dot [24] hosted in a GaAs cantilever. These mechanical oscillators have resonant frequencies below 6 MHz and thus high phonon occupancies even at cryogenic temperatures. Cooling mechanical motion can be achieved using a variety of techniques [25], including laser cooling [26]. However, these techniques are often incompatible with qubit operation, for example due to substrate heating [27]. The challenge resides in realising spin-to-motion coupling in a mechanical resonator exhibiting large quality factors and a large resonance frequency, so that the quantum regime can be accessed at dilution refrigerator temperatures. Due to their small mass and unique material properties, carbon nanotubes (CNTs) can realise resonators with quality factors of over

* These authors contributed equally to this work.

† natalia.ares@eng.ox.ac.uk

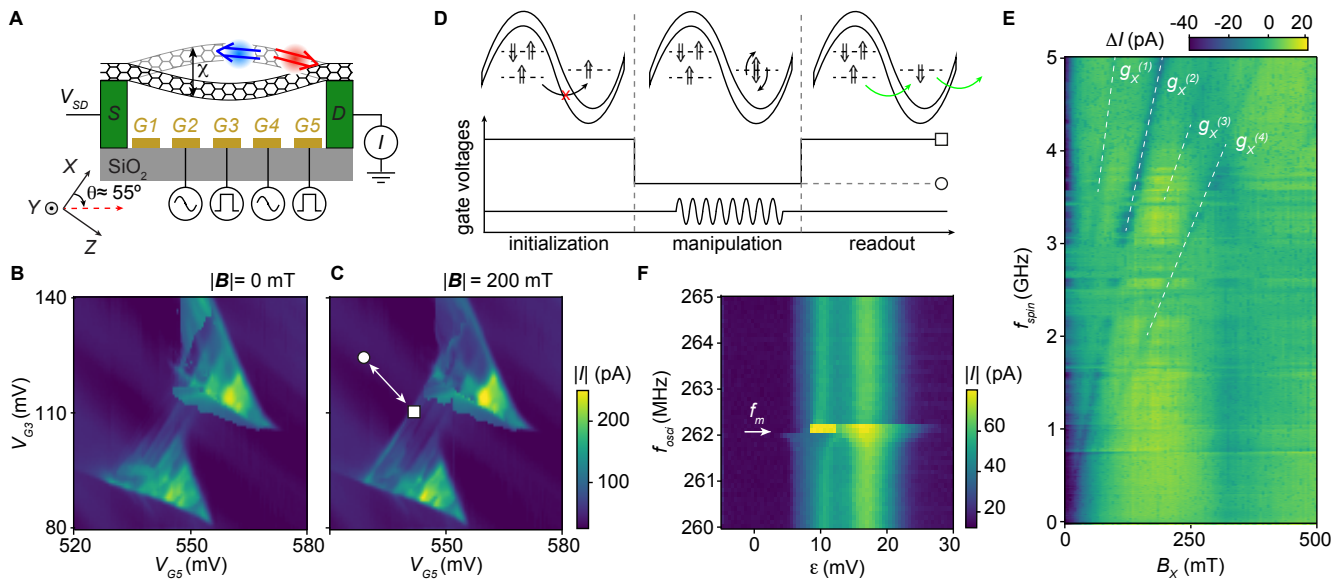


Fig. 1. Determination of spin-valley and mechanical frequencies. (A) The carbon nanotube is suspended between source and drain contacts, and over five gate electrodes, G1-G5. We measure a current I through the device against a source-drain voltage V_{SD} . A magnetic field B_X is applied along the X direction, and the CNT is oriented at an angle θ of approximately 55° against the X axis. A double dot confined along the CNT (see red and blue double-arrows) allows us to define a spin-valley qubit and to use Pauli spin blockade for readout. The CNT motion oscillates with an amplitude χ as a response to a drive tone at frequency f_{osci} in one of the gates. (B) and (C) show the absolute value of the current $|I|$, measured as a function of gate voltages V_{G3} and V_{G5} at a Pauli-blocked transition. Other voltages are $V_{SD} = -4$ mV, $V_{G1} = V_{G2} = V_{G4} = 0$ V, and the applied field magnitude is $|B| = 0$ mT and $|B| = 200$ mT, respectively. The square (circle) indicates the initialization/readout (manipulation) gate voltages and the arrow marks the pulse axis, see schematic D. (D) Pulse scheme for qubit initialization, qubit manipulation, and detection of EDSR. Upper panel: Double-dot occupations indicating that Pauli spin blockade makes the current sensitive to the spin-valley state (double-arrows). Lower panel: Cycle of gate voltage pulses for qubit initialisation, qubit manipulation, and detection of EDSR. The qubit is driven with a microwave pulse at frequency f_{spin} . (E) Resonant signal ΔI as a function of drive frequency f_{spin} and applied field B_X . The pulse cycle used is that in panel D and the microwave power P_{spin} was -33 dBm at the device (here applied to G4). The average current in each row is subtracted to highlight the EDSR resonances (f_{EDSR}). Resonances appear as dark lines (dashed white lines are a guide to the eye). Landé g -factor values corresponding to these resonances are shown. (F) Observation of the nanotube’s mechanical frequency (f_m), identified at ca. 261.9 MHz, by measuring the current I as a function of double dot detuning (ϵ) while sweeping f_{osci} . The drive power P_{osci} (applied to G4) is -33 dBm at the device and the field is $B_X = 200$ mT. Note that the detuning start point and axis are different than those indicated in panel C. No EDSR excitation was applied for this measurement.

a million [28] and resonant frequencies of up to 39 GHz [29]. This type of device allows for quantum dots to be defined electrostatically [30, 31]. The coupling between single-electron tunneling and the CNT motion was recently estimated and it was found to reach the ultra-strong coupling regime [32, 33]. Strong coupling of single spins to mechanical motion was predicted [34], but never observed.

Here, we report on the first observation of coupling between a single spin and mechanical motion at radio frequencies. The single spin is confined in a quantum dot which is electrostatically defined in a fully suspended carbon nanotube. It is driven by EDSR and interacts with the nanotube’s motion via spin-orbit coupling. We observe this coupling when the Larmor and mechanical frequencies are both, resonant and off-resonant. We develop a theoretical model that captures the dependence of the gyromagnetic tensor on the carbon nanotube displace-

ment, including non-linearities in the nanotube’s motion. Our model can accurately reproduce our observations. The demonstration of spin-mechanical coupling unveils a range of new opportunities, spanning both fundamental and practical applications of quantum mechanics.

The CNT is stamped across metallic contact electrodes to give a vibrating segment of length ~ 900 nm, and is measured at a temperature of 45 mK. Voltages applied to five finger gates beneath the nanotube (labeled $V_{G1}-V_{G5}$) are used to form a double quantum dot (DQD) electrostatically (Fig. 1A). A voltage bias V_{SD} is applied between the leads to drive a DC current I . Both p-p and p-n double-dot configurations are accessible. We focus on the charge transition $(N,1) \rightarrow (N+1,0)$ in a p-n configuration. Since a p-n bandgap only seems present for the right dot (see Methods), we can only assign absolute charge occupations to the right dot and relative charge occupations N to the left dot.

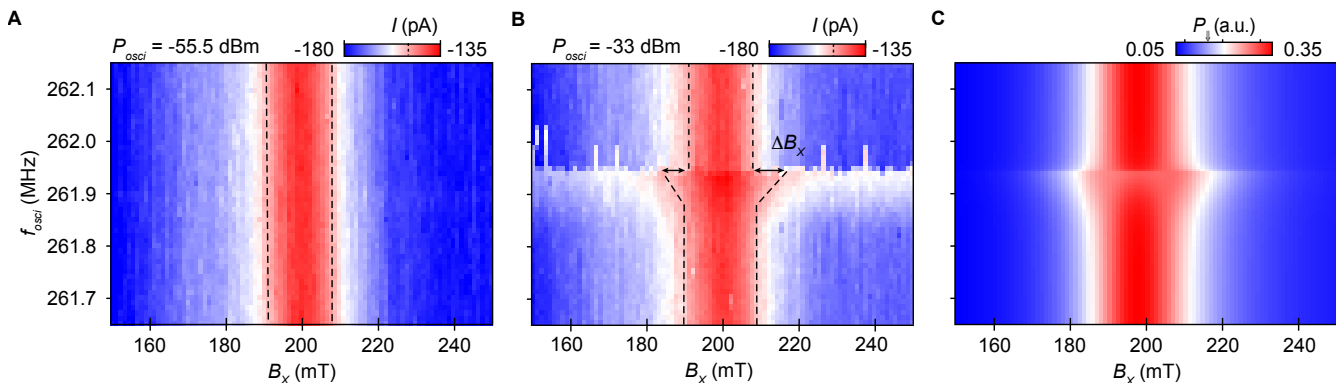


Fig. 2. **Off-resonant coupling between a spin-valley qubit and mechanical motion.** (A-B) Measured EDSR resonance at a field $B_X \approx 200$ mT corresponding to a drive at $f_{\text{spin}} \sim 5.1$ GHz, while the carbon nanotube motion is excited (at G2) at frequencies f_{osci} in the range [261.7, 262.1] MHz. The resonance is the one with g -factor $g_X^{(2)}$ in Fig. 1. Here the spin manipulation is performed using a continuous microwave drive (at G4) with power $P_{\text{spin}} = -34.5$ dBm. Panels A and B correspond to different mechanical drive powers P_{osci} , -55.5 dBm and -33 dBm, respectively. For the larger value of P_{osci} (panel B), we observe EDSR resonance broadening (ΔB_X^{EDSR} indicated by arrows) at $f_m \sim 261.9$ MHz, the frequency corresponding to the mechanical resonance. To quantify this broadening, we pinpoint the values of B_X corresponding to a reduction of $1/\sqrt{2}$ of EDSR current value (dashed black lines). Panel C shows the calculated transition probability P_{\downarrow} from the blocked to the unblocked state, time-averaged until the steady state is reached. The transition probability is obtained by solving the dynamics of Hamiltonian (2) up to first order in χ (with $\lambda_1 = 433$ neV/nm) plus the EDSR driving tone, and including decoherence effects due to the environment (see Methods for details). Our simulation reproduces the EDSR broadening observed in panel B.

With an external magnetic field B_X , Pauli spin blockade is observed as an enhancement of the triangle baseline due to selection rules on spin and valley states (Fig. 1B,C). Pauli spin blockade is identified by a suppression instead of an enhancement of the triangle baseline, with the latter signature found only in systems with strong-spin orbit coupling [35–38]. A cycle of gate voltage pulses applied to G3 and G5, see Fig. 1D, is used to define and control a spin-valley qubit using electrically driven spin resonance (EDSR) [39]. First, an effective triplet state is initialized by configuring the double dot in Pauli spin blockade. Then, G3 and G5 are pulsed to set the double dot in Coulomb blockade, and a microwave burst applied to either G2 or G4 manipulates the spin-valley state. Gate voltages G3 and G5 are pulsed back to the Pauli spin blockade configuration. If the spin-valley state was flipped during the microwave burst, Pauli spin blockade is lifted and the current changes. The pulse cycle is set at $1 \mu\text{s}$. The resulting change in current ΔI as a function of the frequency of the microwave burst f_{spin} and magnetic field B_X is shown in Fig. 1E. Dips in ΔI appear as diagonal lines indicating a resonance when f_{spin} matches the qubit frequency f_{EDSR} . From the slopes of these diagonal lines, we extract effective g -factors: $g_X^{(1)} = (3.30 \pm 0.30)$, $g_X^{(2)} = (1.84 \pm 0.02)$, $g_X^{(3)} = (1.31 \pm 0.06)$ and $g_X^{(4)} = (0.94 \pm 0.01)$. Errors reflect the uncertainty of a linear fit to the EDSR resonances. These multiple EDSR resonances $g_X^{(j)}$ can be attributed to transitions within different subsets of spin-valley states ($g_X^{(1)}$ and $g_X^{(3)}$), as

well as higher harmonics ($g_X^{(2)}$ and $g_X^{(4)}$). We actuate vibrations by injecting a radio-frequency (RF) tone with driving power P_{osci} to either G2 or G4. An abrupt change in I is observed when the frequency of the mechanical drive tone f_{osci} is close to the resonance frequency of the mechanical resonator at ca. $f_m = 261.9$ MHz (Fig. 1F).

In order to evidence the spin-mechanical coupling, we monitor the EDSR resonance while actuating the nanotube’s motion (Fig. 2A, B). Specifically, we fixed f_{spin} at 5.1 GHz, thus driving the EDSR resonance corresponding to $g_X^{(2)}$ in the vicinity of $B_X^{\text{EDSR}} = 200$ mT, and swept f_{osci} in a range of frequencies around f_m . For large enough values of P_{osci} , we observe a broadening ΔB_X of the EDSR resonance at $f_{\text{osci}} \sim f_m$. To quantify this broadening we identify the values of B_X for which the current drops from the maximum EDSR current value by a factor of $1/\sqrt{2}$. The dependence of the broadening ΔB_X on the power P_{osci} is discussed further in the Methods. We observe that the broadening ΔB_X starts at slightly lower frequencies and hits the maximum at f_m . In contrast, for frequencies slightly larger than f_m , no broadening is observed. This asymmetry becomes more evident as P_{osci} increases, indicating the presence of non-linearities in the mechanical motion. For instance, mechanical resonance hardening, i.e. an increase of f_m , and the occurrence of current switches that might be revealing mechanical bistabilities, are further evidence that mechanical non-linearities are present (see Methods). It is important to note that for Fig. 2A, B, f_{osci} is swept from high to low frequencies.

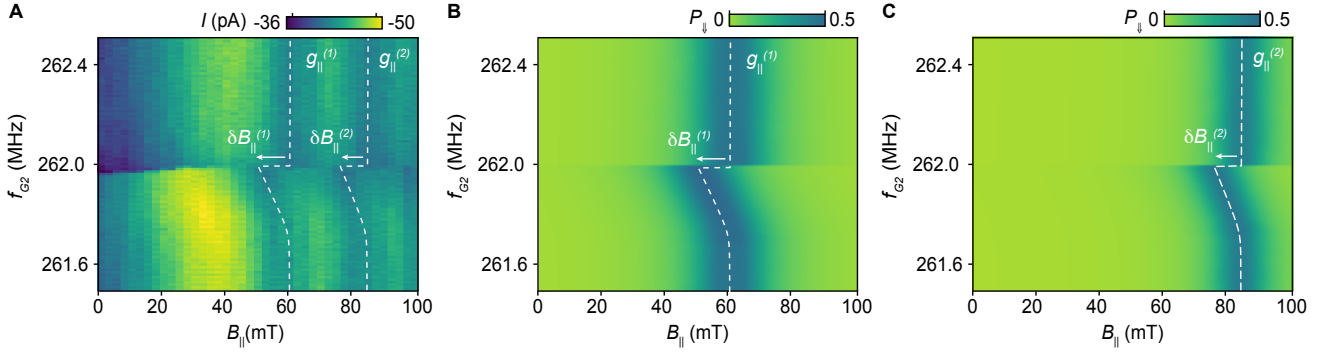


Fig. 3. **Resonant coupling between a single spin and mechanical motion.** (A) Measured resonant signal I as a function of the applied parallel field $B_{||}$ and a single drive frequency f_{G2} at power $P_{G2} = -33$ dBm. The white dashed lines are a guide to the eye for the EDSR resonances. For values of f_{G2} far from f_m , these resonances corresponds to g -factors of $g_{||}^{(1)}$ and $g_{||}^{(2)}$. At f_{G2} slightly below $f_m = 261.9$ MHz, the EDSR resonances shift significantly towards lower values of $B_{||}$. White arrows indicate these shifts, $\delta B_{||}^{(1)}$ and $\delta B_{||}^{(2)}$. Here I is detected by chopping the drive signal applied via $G2$ at 83.1 Hz and locking into the chopper signal [40]. (B)-(C) Calculated transition probability P_{\downarrow} from the blocked to the unblocked state, time-averaged until the steady state is reached. The transition probability is obtained by solving the dynamics of Hamiltonian (2) up to second order in χ plus the EDSR driving tone, and including decoherence effects due to the environment (see Methods for details). Our simulation for the $g_{||}^{(1)}$ and $g_{||}^{(2)}$ resonances reproduce the EDSR resonances observed in panel A.

We model the impact of the interaction between the mechanics and the spin-valley qubit as a modulation of the qubit frequency f_{EDSR} . The qubit is subjected to the applied magnetic field B_{χ} with components parallel ($B_{||}$) and perpendicular (B_{\perp}) to the CNT's axis at zero displacement. The presence of spin-orbit coupling may induce an anisotropic gyromagnetic tensor [34], $\mathbf{g}^{(j)}$, with components $g_{||}^{(j)}$ and $g_{\perp}^{(j)}$, where the superscript j indicates the different spin-valley resonances observed in figure 1E and their associated resonances. For the CNT at rest, the qubit Hamiltonian for a given pair of spin-valley states is

$$H_{\text{rest}} = \frac{1}{2} \mu_B \sqrt{B_{||}^2 g_{||}^2 + B_{\perp}^2 g_{\perp}^2} \sigma_3, \quad (1)$$

where σ_3 is the Pauli operator in the energy quantisation axis of the qubit. When the mechanical motion is driven, the CNT displaces with an amplitude χ and $B_{||}$ and B_{\perp} in Eq. (1) can be modified as follows: $B_{||} \rightarrow (B_{||} \ell - B_{\perp} \chi) / \sqrt{\chi^2 + \ell^2}$, and $B_{\perp} \rightarrow (B_{\perp} \ell + B_{||} \chi) / \sqrt{\chi^2 + \ell^2}$, where ℓ is the distance between the qubit and the closest lead. For small oscillation amplitudes χ , we then expand to second order and obtain the qubit Hamiltonian

$$H = H_{\text{rest}} + \lambda_1 \chi \sigma_3 + \lambda_2 \chi^2 \sigma_3, \quad (2)$$

where λ_1 and λ_2 are corrections to the qubit frequency that depend on $g_{||}$, g_{\perp} , and the field orientation (see Methods).

Using Eq. (2) we can calculate the steady-state qubit transition probability P_{\downarrow} to the unblocked state that is proportional to the current flowing through the CNT,

I . Given the signatures of mechanical non-linearities observed in Figs. 2A and B, we consider a Duffing model for the mechanics, see Methods. Fig. 2C shows P_{\downarrow} estimated from the Hamiltonian corresponding to Eq. (2) up to first order, with $\lambda_1 = 433$ neV/nm. Including just the first order correction in χ the model captures the physics of the off-resonant experiment, see Fig. 2B. We thus conclude that the main effect of the off-resonant coupling between the spin-valley qubit and the mechanical motion is a broadening of the EDSR resonance. The broadening of f_{EDSR} is governed by the product of the coupling strength and the mechanical amplitude $\lambda_1 \chi / h$, where h is the Planck constant.

So far we have demonstrated spin-mechanical coupling by measuring the broadening $\Delta B_{\chi}^{\text{EDSR}}$ of the EDSR peak at f_m , see Fig. 2. This was achieved in an off-resonant regime, $f_{\text{EDSR}} > f_m$. The model developed to account for spin-mechanical coupling, see Eq. (2), considers a modulation of the Zeeman Hamiltonian that depends on the magnetic field orientation and the g -factor anisotropy. To further test the nature of this coupling, we now align the magnetic field with the CNT axis. Our model in Eq. (2) predicts that the first order correction $\propto \lambda_1$ is switched off and the Zeeman energy modulation is now dominated by the term quadratic in χ (see Methods). Moreover, for this magnetic field orientation, we are able to access the resonant spin-mechanical coupling regime, i.e. $f_{\text{EDSR}} \sim f_m$. This is because in this orientation, the g -factor's value is reduced, thus shifting the EDSR resonance condition for f_m to higher fields where Pauli spin blockade is not lifted. At the resonance condition, we can drive *both* the EDSR resonances and the mechanical motion with a single tone applied to $G2$, f_{G2}

$$(f_{\text{osci}} = f_{\text{spin}} = f_{G2}).$$

In Fig. 3A we display the EDSR resonances corresponding to g-factors $g_{\parallel}^{(1)} = 0.31 \pm 0.03$ and $g_{\parallel}^{(2)} = 0.22 \pm 0.02$ (these are the g-tensor components aligned with the CNT axis, while those in Fig. 1E are the X-aligned components). For $f_{G2} \sim f_m$, we observe a shift of the EDSR resonances, $\delta B_{\parallel}^{(j)} = B_{\parallel}^{(j)}(f_m + \epsilon) - B_{\parallel}^{(j)}(f_m - \epsilon)$ for small $\epsilon > 0$ with $j = 1, 2$. These shifts show a strong asymmetry: at frequencies f_{G2} smaller than f_m , the EDSR resonance is shifted to lower field strengths, reaching the maximum shift at f_m . In contrast, for frequencies only slightly larger than f_m , no shift is observed. (Note that for Fig. 3A, f_{G2} is swept from high to low frequencies.)

To model the observed frequency shift, we now require in Eq. (2) the second-order correction that arises from the spin-mechanical coupling. For each EDSR resonance, this is given by

$$\lambda_2 = E_{\text{rest}} \frac{g_{\perp}^2 - g_{\parallel}^2}{4\ell^2 g_{\parallel}^2}, \quad (3)$$

where E_{rest} is the energy gap of H_{rest} , see Eq. (1) and Methods for details. The time average effect of this coupling is to produce an effective qubit frequency given by

$$f_{\text{eff}} = \frac{\mu_B}{h} g_{\parallel} B_{\parallel} + \frac{1}{2h} \lambda_2 A^2(f_{G2}), \quad (4)$$

where $A(f_{G2})$ is the frequency response of the mechanical oscillator considering the Duffing non-linearity. This expression allows us to extract the value $\lambda_2 A_{\text{max}}^2$, with A_{max} the maximum displacement, from the fit of the EDSR resonances from Fig. 3A (white dashed line). Fig. 3B shows the simulation of the transition probability using the parameters obtained from the fit of Eq. (4). We find that the experimental measurements, Fig. 3A, are extremely well matched with the theoretical model, Fig. 3B and C. This agreement unequivocally proves that the observed frequency shift in the resonance is due to spin-mechanical coupling.

The fit of λ_2 together with Eq. (3) allows us to make a quantitative prediction of the g_{\perp} coefficient. Here one needs to include an estimate of the qubit's position ℓ on the CNT, which is ca. 900 nm long. For a reasonable range of ℓ , i.e. $\ell=50 - 250$ nm, we find $g_{\perp}=4 - 24$. Note, that the coupling corrections λ_1 and λ_2 are field-orientation dependent. However, having found the two g-tensor values, g_{\parallel} and g_{\perp} , we can now determine these corrections for *arbitrary* field orientations. In particular, for the magnetic field applied along the X direction, we find $\lambda_1 = 380 - 455$ neV/nm. This result is consistent with the value of 433 neV/nm used in the simulation of Fig. 2C.

Here we have demonstrated spin-orbit-mediated coupling of a spin-valley qubit to high-frequency motion using a suspended carbon nanotube device. As seen in

Figs. 2 and 3, coupling is possible both when the qubit and mechanics are off-resonant, as well as when they resonate at the same frequency. The excellent theory-experiment match allows us to fully map out the coupling mechanism at play. By probing this coupling for two different orientations of the applied magnetic field, we uncover that the coupling strength is strongly affected by the g-factor anisotropy. We also give a first experimental estimate of the strength λ_1 of the spin-mechanical coupling.

The spin-mechanical coupling we demonstrate unlocks a realm of experiments combining single spin qubits with a linear or non-linear, classical or quantum resonator. A single spin coupled to a quantum resonator acting as a battery allows, for example, the exploration of quantum batteries [41–43], quantum Maxwell demons [44] and thermodynamic engines [45]. For highly coherent spin states [46], spin-mechanical coupling would allow for work extraction from quantum coherence [47] and the realisation of macroscopic states of motion [48]. It could also enable ground-state cooling of a macroscopic resonator by spin-polarized currents [49]. The coupling of high-frequency mechanics and spin offers novel approaches for high-efficiency microwave-to-optical conversion [50] and long-range coupling of spin qubits [3, 6]. Mechanical resonators are smaller in size compared to their superconducting counterparts and their properties are not degraded in the presence of strong magnetic fields, enabling the realisation of large networks consisting of interconnected spin qubit registers.

ACKNOWLEDGMENTS

We thank D. Zumbühl, E. Laird and G. J. Milburn for stimulating discussions on the subject of this research. This research was supported by grant number FQXi-IAF19-01 from the Foundational Questions Institute Fund, a donor-advised fund of the Silicon Valley Community Foundation. NA acknowledges the support from the Royal Society (URF-R1-191150), EPSRC Platform Grant (grant number EP/R029229/1) and the European Research Council (ERC) under the European Union's Horizon 2020 research and innovation programme (grant agreement number 948932). AP Acknowledges support from the HUN-REN Hungarian Research Network, by the Ministry of Culture and Innovation and the National Research, Development and Innovation Office (NKFIH) within the Quantum Information National Laboratory of Hungary (Grant No. 2022-2.1.1-NL-2022-00004), and by NKFIH via the OTKA Grant No. 132146. JM acknowledges funding from the Swedish Vetenskapsrådet, Swedish VR (Project No. 2018-05061). JA acknowledges support from EPSRC (EP/R045577/1), and thanks the Royal Society for support.

METHODS

Device fabrication

The carbon nanotube (CNT) used in this experiment has been grown by chemical vapor deposition and then transferred via flip-chip stamping on a silicon chip. For the CNT synthesis, we deposit a FeCl₃ catalyst mixed with PMMA on a quartz substrate with etched pillars. The CNT are then grown in a furnace with a CH₄/H₂ atmosphere diluted to 20% concentration in Argon at 950 °C. After the growth, the CNTs are transferred to the device chip by stamping using an optical mask aligner. The device layout consisting of two 110 nm tall Cr/Au pillars and five 18 nm tall Cr/Au gate electrodes was realised on the silicon substrate using standard electron beam lithography followed by thermal evaporation of Cr/Au gates. All five gates underneath the CNT are connected to bias tees that allow the application of DC and high bandwidth AC voltages. The length and the radius of the CNT used for this experiment have not been measured directly, however these parameters have been estimated from previous experiments and found to be, respectively, 936 ± 10 nm and 3.9 ± 0.2 nm, see Ref. [32]. The device was measured inside a Triton 200 cryofree dilution refrigerator with a base temperature of 45 mK, and equipped with a vector magnet that could generate 6 T along the cryostat main axis, defined as Y in the laboratory frame of coordinates, and 1 T along the remaining axis X and Z.

Forward bias EDSR and Qubit location

To confirm the EDSR signal, we measured it at a different charge transition with opposite source drain bias. In Extended Data Fig. 1A we present a stability diagram. As a function of V_{G5} , starting from the lower corner, we observe a transition to a double dot regime suggesting the presence of a bandgap for the right dot (highlighted by a white shade) [51]. We therefore identify two transport-type regions p-p and p-n, which allow us to assign the p-n charge occupation $(N, 1)$ - $(N-1, 0)$ to the pair of bias triangles shown in Fig. 1B-C of the main text and here highlighted by the dashed white box. As shown in the main text, this transition exhibits Pauli-blockade when transport is measured using a negative source-drain bias. On the other hand, the pair of triangles highlighted by the dashed red box marks the transition $(N+1, 2) \rightarrow (N, 1)$. Extended Data Fig. 1B-C shows Pauli blockade at this particular pair of bias triangles measured with a source-drain bias of $V_{SD} = +4$ mV. Similar to Fig. 1B of the main text, at $B_X = 0$ mT, the current at the base of the lower left bias triangle is suppressed by Pauli blockade, see the red dash box in Extended Data Fig. 1B. Measuring the current within this region in the presence

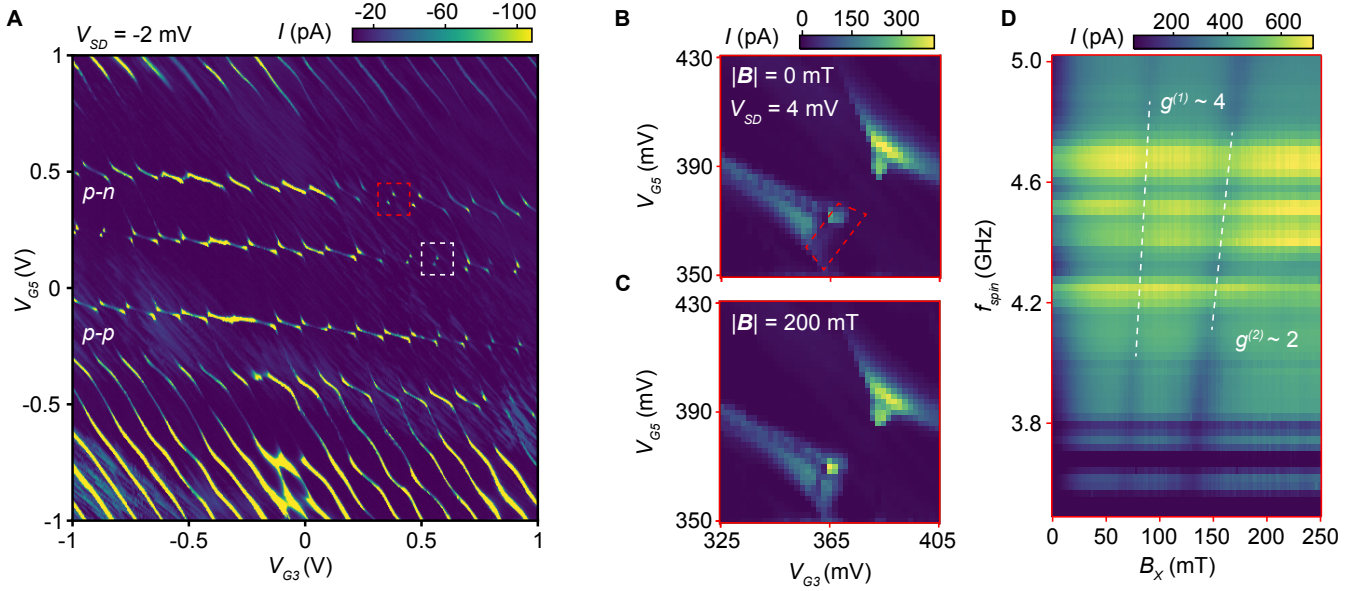
of a continuous wave excitation f_{spin} , reveals the EDSR spectrum presented in Extended Data Fig. 1D. Consistent with the data presented in the main text, even in forward bias the two observed EDSR resonances are evident as regions of suppressed currents with estimated g -factors of 2 and 4 respectively. We find that this observation, considering that no EDSR was detected outside either of the Pauli-blockaded regions, confirms that we can define spin qubits in our CNT device.

Magneto transport spectroscopy and EDSR as a function of field orientation

Extended Data Fig. 2A shows magneto transport spectroscopy measured as a function of gate voltage V_{G5} and field orientation in the X-Z plane of our reference frame (see Fig. 1A in the main text.) Throughout this measurement, we fixed the magnetic field magnitude to 500 mT, and set V_{G3} in order to probe the region of current rectified by Pauli blockade as a function of V_{G5} . As a function of the field angle θ , we observe two regions of suppressed current with 180° periodicity at angles $\theta = 55^\circ$ and 235° , and angles 145° and 235° . We attribute the regions of strongest (weakest) current suppression to the direction for which the field aligns parallel or anti-parallel with (perpendicular to) the main axis of the carbon nanotube. Extended Data Fig. 2B shows EDSR resonances measured with the field oriented along the X direction of the reference frame. Extended Data Fig. 2C shows EDSR resonances measured with the field oriented along the direction of strongest current suppression, which we labeled B_{\parallel} (see the white dashed line in panel A at $\theta = 55^\circ$).

Power dependence of the spin mechanical coupling

In Extended Data Fig. 3, we show additional data displaying the off-resonant spin mechanical coupling as a function of the mechanical drive power P_{osci} . From panels A to E, P_{osci} is stepped from -55.5 dBm to -30.5 dBm, with panels A and D corresponding respectively to the data presented in Fig. 2A and 2B of the main text. With increasing P_{osci} , we observe a broadening (ΔB_X) of the EDSR resonance when $f_{\text{osci}} \sim f_m$. The broadening is obtained by comparing the width of the EDSR at $f_{\text{osci}} = 261.65$ MHz, with its width at $f_{\text{osci}} = f_m$. Here, the width is defined as the range of field values where the current I is within a factor $1/\sqrt{2}$ larger than the minimum EDSR current (see white dashed lines). In panel F top we plot the estimated (ΔB_X) divided by 2, as a function of the drive power P_{osci} and the corresponding carbon nanotube displacement δz . As discussed in the main text, the broadening shows a non-linear dependence on the driving power, an effect of the nonlinear nature of the



Supplementary Fig. 1. **Pauli spin blockade and EDSR spectrum for a different charge transition.** (A) Charge stability diagram of the double quantum dot measured as a function of V_{G3} and V_{G5} with $V_{SD} = -2$ mV. As a function of V_{G5} we can tune the system into a double quantum dot. The white dash box indicates the pair of bias triangles used in the main text (see Fig. 1B-C), which shows Pauli blockade at negative source-drain bias. Similarly, in panels B and C we show the current measured with positive bias $V_{SD} = +4$ mV, probed in the vicinity of the bias triangles at the $(N-1, 2) \rightarrow (N, 1)$ transition (see red dashed box), at different magnetic fields magnitudes $|\mathbf{B}| = 0$ mT and $|\mathbf{B}| = 200$ mT respectively. At zero magnetic field the current at the base of the lower left bias triangle is suppressed by Pauli blockade, see the red dashed box in panel B. (D) EDSR spectrum as a function of the drive frequency f_{spin} and applied field B_x . Like the data presented in the main text, we identify two EDSR resonances as regions of suppressed current with g -factors respectively $g^{(1)} \approx 4$ and $g^{(2)} \approx 2$ (see white dashed lines).

oscillator. In Extended Data Fig. 3G we present further evidence for the nonlinearity of the mechanical oscillator. The current traces as a function of f_{osci} are linecuts extracted from Extended Data Fig. 3A-E and highlight the hardening of the mechanical frequency f_m as a function of P_{osci} . Previous studies on CNT resonators have found these signatures to be consistent with a Duffing oscillator [52, 53]. Recently, Duffing oscillators in CNT resonators have been proposed as a platform to realise nanomechanical qubits [54].

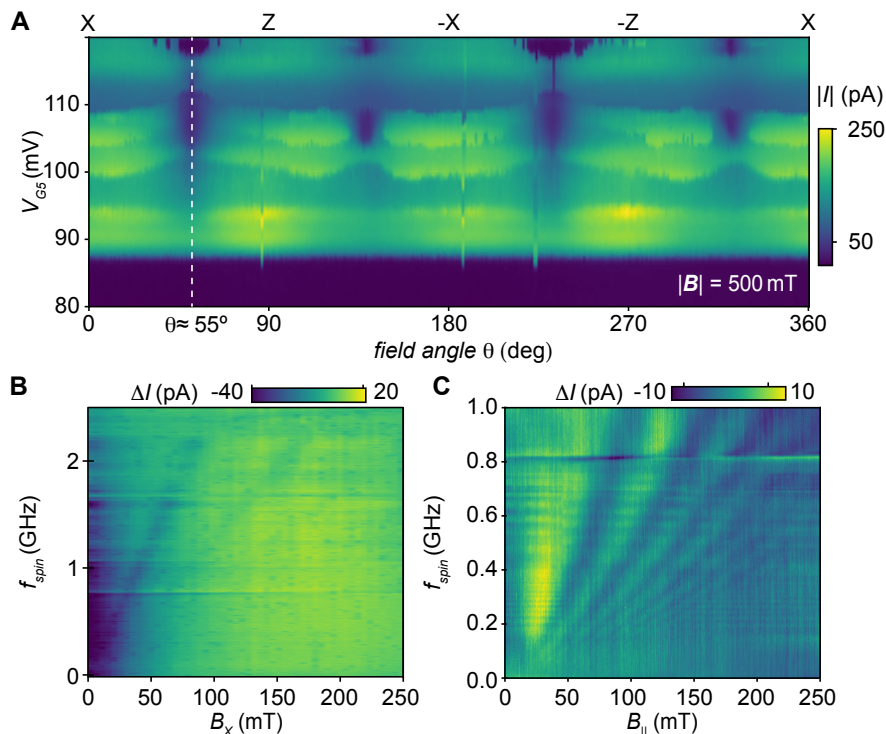
Detuning dependence of the spin mechanical coupling

In Extended Data Fig. 4A we show EDSR resonances measured as a function of drive power P_{G2} and applied field B_{\parallel} with a single drive frequency such that $f_{\text{osci}} = f_{\text{spin}} = f_{G2} = f_m = 261.9$ MHz. This allows us to drive the spin while simultaneously driving the mechanics and investigating the coupling as a function of the driving powers. The fixed frequency driving reveals a fan of EDSR resonances. As a function of P_{G2} we observe a shift in the EDSR resonances towards higher values of the applied field B_{\parallel} . We note that this is in

contrast with the data presented in Fig. 3A of the main text, where the observed EDSR resonances shift towards lower values of the applied field as a function of the drive frequency.

To investigate this further, we take similar measurements at different detuning values. Extended Data Fig. 4B shows the charge stability with circles indicating the detuning corresponding to Extended Data Fig. 4A and Extended Data Fig. 4C to L. Note that the detuning of Fig. 3A in the main text is highlighted with a star. As a function of detuning, we observe a distinct change in the sign of the EDSR resonant shift, with panels C-G exhibiting a shift towards lower values of the applied eternal field, panel H showing no appreciable shift, and panels I, L, and A showing a marked shift toward higher values of magnetic field. This change in the sign of the spin-resonance shift indicates that we could in principle tune the coupling between the spin and the mechanical motion. We attribute this tunability to the modulation of the g -tensor components with gate voltages V_{G3} and V_{G5} .

The model employed to explain the origin of the spin-mechanical coupling suggests that in the resonant case, the coupling parameter λ_2 depends on the difference of the squares of the g -factors components, g_{\perp} and g_{\parallel} . This



Supplementary Fig. 2. **Magneto transport angular dependence and EDSR at different field orientations.** (A) Current measured as a function of V_{G5} and the angle θ which determine the magnetic field orientation in the XZ plane in our frame of coordinates. The magnitude of the magnetic field was kept constant at 500 mT. Supported by geometrical considerations, we identify these regions of suppressed current with the directions for which the field aligns along the main carbon nanotube axis. The angle $\theta = 55^\circ$, highlighted by a white dashed line marks the orientation that we called $B_{||}$ in the rest of the manuscript. (B) EDSR resonances measured with the field aligned along the X -axis of our reference frame (adapted from Fig. 1E of the main paper). (C) EDSR resonances measured at the field orientation $B_{||}$.

can in principle lead to variable coupling strength owing to a modulation of the g -factor components with detuning. g -tensor modulation with gate voltages and applied magnetic field has been observed in a variety of materials including SiGe quantum dots [55], Ge/SiGe heterostructures [56], and CMOS silicon on insulator quantum dots devices [57, 58].

Theoretical model

The Hamiltonian of the spin-valley qubit in the presence of a magnetic field \mathbf{B} is in general given by

$$H_0 = \frac{1}{2} \mu_B \mathbf{B} \cdot \mathbf{g} \cdot \boldsymbol{\sigma}, \quad (5)$$

where \mathbf{g} is the anisotropic g -tensor [59, 60]. The off-and-on resonance experiments described in the main text were performed with two different field orientations on a plane containing the CNT. As such, without loss of generality, we define a parallel ($B_{||}$) and perpendicular (B_{\perp}) component of the magnetic field to the CNT at rest, so that the third component of \mathbf{B} is zero for all

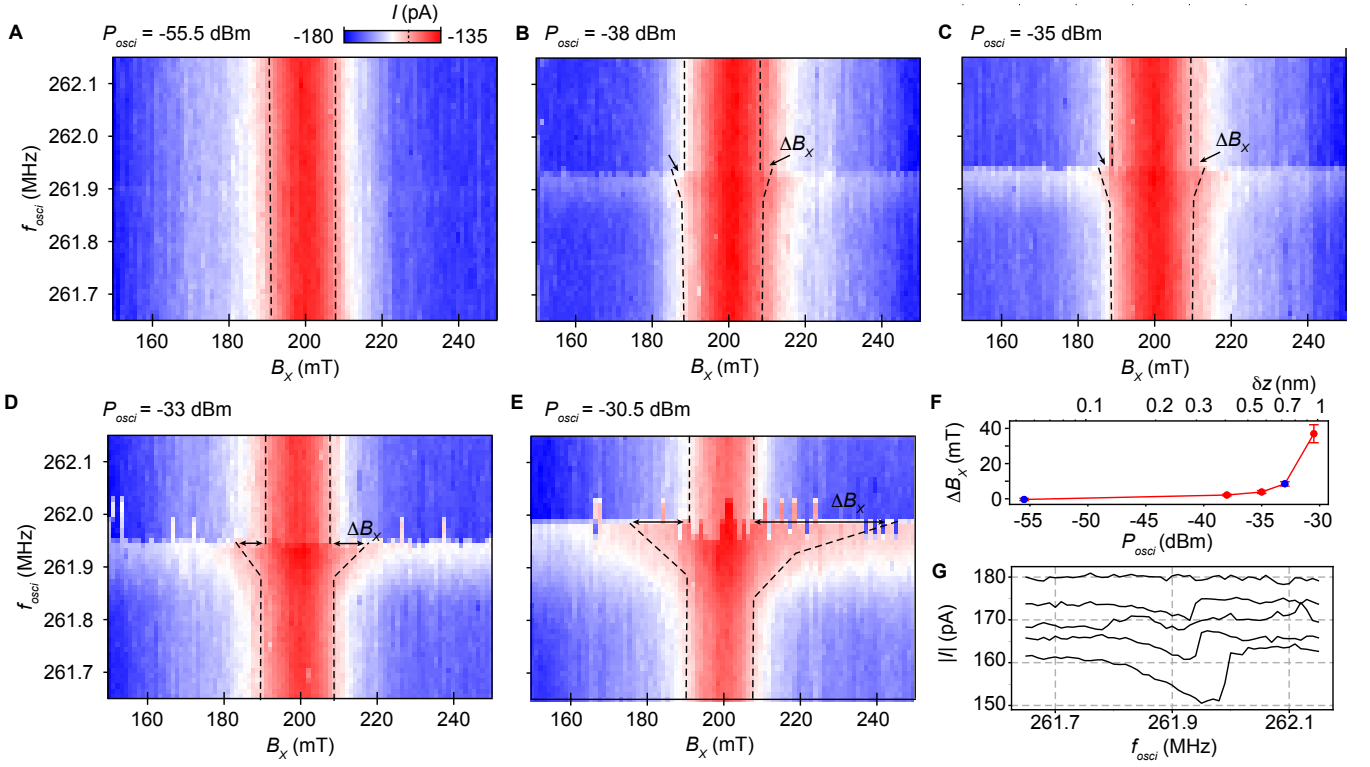
measurements. The Hamiltonian for the CNT at rest is then given by

$$\begin{aligned} H_{\text{rest}} &= \frac{1}{2} \mu_B (B_{||} g_{||} \sigma_{||} + B_{\perp} g_{\perp} \sigma_{\perp}) \\ &= \frac{1}{2} \mu_B \sqrt{B_{||}^2 g_{||}^2 + B_{\perp}^2 g_{\perp}^2} \sigma_3 = \frac{1}{2} E_{\text{rest}} \sigma_3, \end{aligned} \quad (6)$$

where σ_3 is the Pauli operator in the direction of the energy quantisation axis of the qubit.

If the CNT oscillates within this same plane defined by magnetic field orientations $B_{||}$ and B_{\perp} , then under a displacement χ of the CNT, the parallel and perpendicular field components, with respect to the CNT main axis, rotate by an angle $\tan \theta = \ell/\chi$, where ℓ is the distance of the quantum dot to the closest lead (see Fig. 1A of the main text.). The parallel and perpendicular components of the field change according to

$$B_{||} \longrightarrow \frac{B_{||} \ell - B_{\perp} \chi}{\sqrt{\chi^2 + \ell^2}}, \quad B_{\perp} \longrightarrow \frac{B_{\perp} \ell + B_{||} \chi}{\sqrt{\chi^2 + \ell^2}}. \quad (7)$$



Supplementary Fig. 3. **Power dependence of the spin mechanical coupling.** (A)-(E) Non-resonant spin mechanical coupling for increasing mechanical drive power P_{osci} , from -55.5 dBm to -30.5 dBm. Panel A and D are the same as Fig. 2 A-B in the main text. With increasing values of P_{osci} , the EDSR resonance broadens (ΔB_x indicated by arrows) while approaching the mechanical resonance frequency f_m (see panel F top). Seemingly, with increasing driving power the mechanical resonance shifts to higher frequencies due to the non-linearity of the mechanical oscillator. (F) Broadening of the EDSR resonance peak at $f_{\text{osci}} \sim f_m$ as a function of the mechanics driving power P_{osci} . The blue dots indicate the estimated broadening of the data presented in the main text. On the top axis, we report the overall nanotube displacement δz estimated from P_{osci} using a standard electrostatic model with the CNT mass, physical dimensions, and capacitance to the electrostatic gates are obtained from previous experiments [32]. (G) Linecuts extracted from A to E going from top to bottom (traces are offset for clarity), at $B_x = 185$ mT, showing the current as a function of f_{osci} , for different excitation powers.

The Hamiltonian in the new quantisation axis is then

$$H_0 = \frac{1}{2} \mu_B \sqrt{\frac{(B_{\parallel} \ell - B_{\perp} \chi)^2 g_{\parallel}^2}{\chi^2 + \ell^2} + \frac{(B_{\perp} \ell + B_{\parallel} \chi)^2 g_{\perp}^2}{\chi^2 + \ell^2}} \sigma_3. \quad (8)$$

Expanding to the second order in χ we then have

$$H_0 = \frac{1}{2} E_{\text{rest}} \sigma_3 + \lambda_1 \chi \sigma_3 + \lambda_2 \chi^2 \sigma_3, \quad (9)$$

where

$$\lambda_1 = \mu_B^2 \frac{B_{\perp} B_{\parallel} (g_{\perp}^2 - g_{\parallel}^2)}{2 \ell E_{\text{rest}}}, \quad (10)$$

$$\lambda_2 = \mu_B^4 \frac{(B_{\parallel}^4 g_{\parallel}^2 - B_{\perp}^4 g_{\perp}^2) (g_{\perp}^2 - g_{\parallel}^2)}{4 \ell^2 E_{\text{rest}}^3}. \quad (11)$$

We will here consider the mechanics as a classical system and hence χ will be a classical displacement satisfying the equations of motion of a Duffing oscillator [52–54],

that is

$$\ddot{\chi} + \nu \dot{\chi} + \omega_m^2 \chi + \beta \chi^3 = \frac{F_0}{m} \cos(\omega_d t), \quad (12)$$

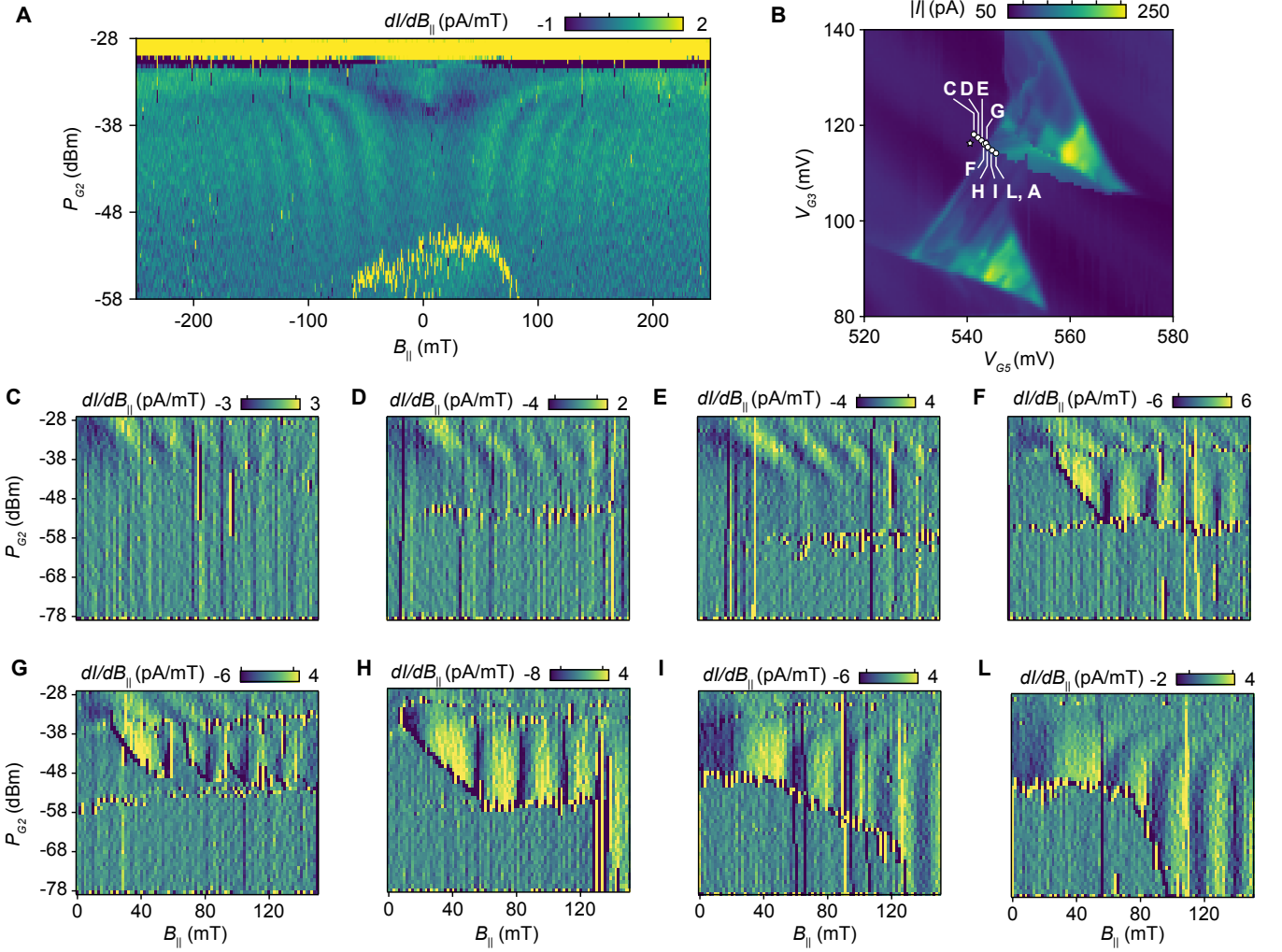
where ν is the damping coefficient of the mechanics, β the Duffing coefficient, F_0 the driving force, and m the mass of the CNT. To deal with the Duffing equation analytically or numerically it is very convenient to rewrite the equations of motion in dimensionless quantities

$$\begin{aligned} \bar{t} &= t \omega_m, & \bar{\omega} &= \frac{\omega}{\omega_m}, & \bar{\chi} &= \frac{m \omega_m^2}{F_0} \chi, \\ \bar{\nu} &= \frac{\nu}{\omega_m}, & \bar{\beta} &= \frac{\beta F_0^3}{m^3 \omega_m^8}. \end{aligned} \quad (13)$$

so that

$$\ddot{\bar{\chi}} + \bar{\nu} \dot{\bar{\chi}} + \bar{\chi} + \bar{\beta} \bar{\chi}^3 = \cos(\bar{\omega} \bar{t}). \quad (14)$$

In what follows we will focus on the case of very weak non-linearity, $\bar{\beta} \ll 1$. In this regime, the response of



Supplementary Fig. 4. **Detuning dependence of the spin-mechanical coupling.** (A) here we show dI/dB_{\parallel} revealing EDSR resonances as a function of applied parallel field B_{\parallel} and drive power P_{G2} at a fixed drive frequency $f_{G2} = 261.9$ MHz. For increasing values of P_{G2} the EDSR resonances shift significantly towards higher values of B_{\parallel} . (B) Charge stability diagram of the double dot with markers indicating the detunings at which panels A and C-L have been measured. The star indicates Fig. 3A in the main text. Panels (C)-(L) show EDSR resonances measured as a function of P_{G2} and B_{\parallel} at $f_{G2} = 261.9$ MHz. Each panel is measured at a different detuning point highlighted by circles in panel B. Like in panel A, we observe a shift in the EDSR resonances as a function of P_{G2} . Similar to Fig. 3A in the main text, in panels C to G the observed shift occurs towards lower values of B_{\parallel} . In panel H we do not observe any appreciable shift, while similar to panel A, panels I and L show the resonances shifting towards higher values of the applied field.

the oscillator is approximately harmonic, with an amplitude given by the frequency-dependent Duffing response. The values of $\bar{\beta}$ extracted from the experimental data and shown in the next section, are consistent with this assumption.

The qubit is further driven by the EDSR pulse, which induces Rabi oscillations. Assuming the condition for the rotating wave approximation (RWA) we then have the effective qubit Hamiltonian

$$H = H_0 + \Omega\sigma_1, \quad (15)$$

where Ω is the Rabi frequency.

Finally, the qubit in the experiment is subject to different sources of noise that induce strong decoherence. To account for this effect, we use a standard pure-dephasing master equation

$$\dot{\rho} = -\frac{i}{\hbar}[H, \rho] + \Gamma(\sigma_3\rho\sigma_3 - \rho), \quad (16)$$

where Γ determines the decoherence time. For the case where decoherence is dominated by pure dephasing [61], we have that $\Gamma \sim 1/T_2^*$.

Off-resonant case

In the off-resonant case, the magnetic field is applied in the direction \mathbf{X} , forming an angle $\theta \approx 55^\circ$ with respect to the direction parallel to the CNT at rest. To model these measurements, we use Eq. (16) with H_0 expanded to first order in χ , see Eq. (9). The simulation of Fig. 2C of the main text is done by time evolving the master equation (16) until steady-state is reached and time-averaging the unblocked state probability. For the simulation, the parameters taken are

$$\lambda_1^{(2)} = 433 \frac{\text{neV}}{\text{nm}}, \quad \bar{\beta} = 2 \times 10^{-12}, \quad (17)$$

$$\Gamma = 392.9 \text{ MHz}, \quad \Omega = 2\pi \times 7.6 \text{ MHz}.$$

The spin-mechanics coupling $\lambda_1^{(2)}$ is chosen to match the observed EDSR broadening observed at the mechanical resonance. The value of $\bar{\beta}$ is set to match the observed asymmetry in the frequency response of the mechanical oscillator, while the values of Ω and Γ are chosen to match the EDSR width. It is worth noting that within the regime of strong decoherence, $\Gamma \gg \Omega$, particularly precise values Ω and Γ are not too relevant. For the calculations corresponding to the simulation displayed in Fig. 2C in the main text only the width of the resonance depends on their value.

Resonant, parallel field case

In the resonant case, the magnetic field is oriented parallel to the CNT at rest. That is, $B_\perp = 0$, $B_\parallel = B$. Substituting into Eq.(10) we see that in this case $\lambda_1 = 0$, i.e. the linear contribution of the mechanics vanishes. Therefore, the lowest order contribution from the mechanics is the quadratic term, and the second coupling takes the simple form given in Eq. (3) of the main text.

As described in the main text, looking at the effective frequency shift produced by the mechanics in this case, we extract the analytical expression for the frequency shift given in Eq. (4) of the main text. We fix the values of the resonance $\omega_m/2\pi = 261.9 \text{ MHz}$, and quality factor to $Q = 5000$ and fit the remaining parameters to the observed frequency shifts. We obtain

$$\bar{\beta} = 2 \times 10^{-11}, \quad \lambda_2^{(1)} \frac{\chi_{\text{max}}^2}{g_\parallel^{(1)} \mu_B} = 9.6 \text{ mT}, \quad (18)$$

$$\lambda_2^{(2)} \frac{\chi_{\text{max}}^2}{g_\parallel^{(2)} \mu_B} = 8.3 \text{ mT},$$

where χ_{max} is the maximum displacement of the CNT, the superscript indicates each of the two resonances observed in Fig. 2C of the main text, and the values of g_\parallel are reported in the main text. It is worth noting that

the value of the Duffing coefficient in this case is not exactly the same as the off-resonant one. This is not surprising as previous works have shown that the Duffing non-linearity in a CNT depends strongly on the applied gate voltages [52, 53].

From the parameters of the CNT and the mechanical driving power P_{osci} we estimate a maximum displacement of 1.5 nm, following the same procedure outlined in the supplementary material of Ref. [32] (with the same parameters). This gives us the second-order coupling constant

$$\lambda_2^{(1)} = 76.5 \frac{\text{neV}}{\text{nm}^2}, \quad \lambda_2^{(2)} = 54.3 \frac{\text{neV}}{\text{nm}^2}. \quad (19)$$

In terms of the zero point motion, the bare second order coupling $\kappa_2^{(k)} = \lambda_2^{(k)} \chi_{\text{zpm}}^2$ is

$$\kappa_2^{(1)} = 2\pi \times 8.5 \text{ Hz}, \quad \kappa_2^{(2)} = 2\pi \times 6.0 \text{ Hz}. \quad (20)$$

-
- [1] D. Rugar, R. Budakian, H. J. Mamin and B. W. Chui Single spin detection by magnetic resonance force microscopy *Nature* **430** 329–332 (2004). <https://doi.org/10.1038/nature02658>
 - [2] G. Balasubramanian, I. Y. Chan, R. Kolesov, M. Al-Hmoud, J. Tisler, C. Shin, C. Kim, A. Wojcik, P. R. Hemmer, A. Krueger, T. Hanke, A. Leitenstorfer, R. Bratschkitsch, F. Jelezko and J. Wrachtrup, Nanoscale imaging magnetometry with diamond spins under ambient conditions, *Nature* **455** 648–651 (2008). <https://doi.org/10.1038/nature07278>
 - [3] P. Rabl, S.J. Kolkowitz, F.H.L. Koppens, J.G.E. Harris, P. Zoller, and M.D. Lukin, A quantum spin transducer based on nanoelectromechanical resonator arrays, *Nature Physics* **6** 602–608 (2010). <https://doi.org/10.1038/nphys1679>
 - [4] S. Kolkowitz, A.C. Bleszynski Jayich, Q.P. Unterreithmeier, S.D. Bennett, P. Rabl, J. G. E. Harris, and M.D. Lukin, Coherent Sensing of a Mechanical Resonator with a Single-Spin Qubit, *Science* **335**, 1603 (2012). <https://doi.org/10.1126/science.1216821>
 - [5] S. J. Whiteley, G. Wolfowicz, C. P. Anderson, A. Bourassa, H. Ma, M. Ye, G. Koolstra, K. J. Satzinger, M. V. Holt, F. J. Heremans, A. N. Cleland, D. I. Schuster, G. Galli, and D. D. Awschalom, Spin–phonon interactions in silicon carbide addressed by Gaussian acoustics, *Nature Physics* **15** 490–495 (2019). <https://doi.org/10.1038/s41567-019-0420-0>
 - [6] E. Rosenfeld, R. Riedinger, J. Gieseler, M. Schuetz, and M.D. Lukin, Efficient Entanglement of Spin Qubits Mediated by a Hot Mechanical Oscillator, *Phys. Rev. Lett.* **126** 250505 (2021). <https://doi.org/10.1103/PhysRevLett.126.250505>
 - [7] W. S. Huxter, M. L. Palm, M. L. Davis, P. Welter, C.-H. Lambert, M. Trassin and C. L. Degen, Scanning gradiometry with a single spin quantum magnetometer, *Nat. Comm.* **13** 3761 (2022). <https://doi.org/10.1038/s41467-022-31454-6>

- [8] F. Tacchino, A. Chiesa, M. D. LaHaye, S. Carretta, and D. Gerace, Electromechanical quantum simulators, *Phys. Rev. B* **97**, 214302 (2018).
- [9] R. A. Thomas, M. Parniak, C. Østfeldt, C. B. Møller, C. Bærentsen, Y. Tsaturyan, A. Schliesser, J. Appel, E. Zeuthen and E. S. Polzik, Entanglement between distant macroscopic mechanical and spin systems, *Nature Physics* **17** 228–233 (2021). <https://doi.org/10.1038/s41567-020-1031-5>
- [10] T. M. Karg, B. Gouraud, C. T. Ngai, G. Schmid, K. Hammerer, P. Treutlein, Light-mediated strong coupling between a mechanical oscillator and atomic spins 1 meter apart, *Science* **369** 174–179 (2020).
- [11] C. G. L. Böttcher, S. P. Harvey, S. Fallahi, G. C. Gardner, M. J. Manfra, U. Vool, S. D. Bartlett and A. Yacoby, Parametric longitudinal coupling between a high-impedance superconducting resonator and a semiconductor quantum dot singlet-triplet spin qubit, *Nat. Comms.* **13**, 4773 (2022). <https://doi.org/10.1038/s41467-022-32236-w>
- [12] N. Didier, J. Bourassa and A. Blais, Fast Quantum Nondemolition Readout by Parametric Modulation of Longitudinal Qubit-Oscillator Interaction, *Phys. Rev. Lett.* **115** 203601 (2015). <https://doi.org/10.1103/PhysRevLett.115.203601>
- [13] N. Aslam, H. Zhou, E. K. Urbach, M. J. Turner, R. L. Walsworth, M. D. Lukin and H. Park, Quantum sensors for biomedical applications, *Nature Reviews Physics* **5** 157–169 (2023).
- [14] B. Gleich, I. Schmale, T. Nielsen, J. Rahmer, Miniature magneto-mechanical resonators for wireless tracking and sensing, *Science* **380** 966–971 (2023).
- [15] B. Pigeau, S. Rohr, L. Mercier de Lépinay, A. Gloppe, V. Jacques, and O. Arcizet, Observation of a phononic Mollow triplet in a multimode hybrid spin-nanomechanical system, *Nat. Comms.* **6**, 8603 (2015). <https://doi.org/10.1038/ncomms9603>
- [16] P. Rabl, P. Cappellaro, M. V. Gurudev Dutt, L. Jiang, J. R. Maze, and M. D. Lukin, Strong magnetic coupling between an electronic spin qubit and a mechanical resonator, *Phys. Rev. B* **79** 041302(R) (2009).
- [17] D. Lee, K. W. Lee, J. V. Cady, P. Ovarthaiyapong and A. C. Bleszynski Jayich, Topical review: spins and mechanics in diamond, *Journal of Optics* **19** 3 (2017).
- [18] A. J. Heinrich, W. D. Oliver, L. M. K. Vander-sypen, A. Ardavan, R. Sessoli, D. Loss, A. Bleszynski Jayich, J. Fernandez-Rossier, A. Laucht and A. Morello, Quantum-coherent nanoscience, *Nature Nanotechnology* **16** 1318–1329 (2021).
- [19] S. Hong, M.S. Grinolds, P. Maletinsky, R.L. Walsworth, M.D. Lukin, and A. Yacoby, Coherent, Mechanical Control of a Single Electronic Spin, *Nano Lett.* **12**, 3920 (2012). <https://doi.org/10.1021/nl300775c>
- [20] P. Ovarthaiyapong, K.W. Lee, B.A. Myers, and A.C. Bleszynski Jayich, Dynamic strain-mediated coupling of a single diamond spin to a mechanical resonator, *Nature Communications* **5**, 4429 (2014). <https://doi.org/10.1038/ncomms5429>
- [21] A. Barfuss, J. Teissier, E. Neu, A. Nunnenkamp, and P. Maletinsky, Strong mechanical driving of a single electron spin, *Nature Physics* **11**, 820 (2015). <https://doi.org/10.1038/nphys3411>
- [22] J. Teissier, A. Barfuss, P. Appel, E. Neu, and P. Maletinsky, Strain Coupling of a Nitrogen-Vacancy Center Spin to a Diamond Mechanical Oscillator, *Phys. Rev. Lett.* **113**, 020503 (2014). <http://dx.doi.org/10.1103/PhysRevLett.113.020503>
- [23] O. Arcizet, V. Jacques, A. Siria, P. Poncharal, P. Vincent, and S. Seidelin, A single nitrogen-vacancy defect coupled to a nanomechanical oscillator, *Nat. Phys.* **7**, 879 (2011). <https://doi.org/10.1038/nphys2070>
- [24] S.G. Carter, A.S. Bracker, G.W. Bryant, M. Kim, C.S. Kim, M.K. Zalalutdinov, M.K. Yakes, C. Czarnocki, J. Casara, M. Scheibner, and D. Gammon, Spin-Mechanical Coupling of an InAs Quantum Dot Embedded in a Mechanical Resonator, *Phys. Rev. Lett.* **121**, 246801 (2018). <https://doi.org/10.1103/PhysRevLett.121.246801>
- [25] M. Aspelmeyer, T.J. Kippenberg, and F. Marquardt, Cavity optomechanics, *Rev. Mod. Phys.* **86**, 1391 (2014). <https://doi.org/10.1103/RevModPhys.86.1391>
- [26] U. Delic, M. Reisenbauer, K. Dare, D. Grass, V. Vuletic, N. Kiesel, M. Aspelmeyer, Cooling of a levitated nanoparticle to the motional quantum ground state, *Science* **367**, 892 (2020). <https://doi.org/10.1126/science.aba3993>
- [27] J. Millen, T. Deesuan, P. Barker, J. Anders, Nanoscale temperature measurements using non-equilibrium Brownian dynamics of a levitated nanosphere, *Nat. Nano.* **9**, 425 (2014). <https://doi.org/10.1038/nnano.2014.82>
- [28] J. Moser, A. Eichler, J. Güttinger, M. I. Dykman, and A. Bachtold, Nanotube mechanical resonators with quality factors of up to 5 million, *Nat. Nano.* **9**, 1007–1011 (2014). <https://doi.org/10.1038/nnano.2014.234>
- [29] E.A. Laird, F. Pei, W. Tang, G.A. Steele, and L.P. Kouwenhoven, A High Quality Factor Carbon Nanotube Mechanical Resonator at 39 GHz, *Nano Lett.* **12**, 193 (2012). <https://doi.org/10.1021/nl203279v>
- [30] J. Waissman, M. Honig, S. Pecker, A. Benyamini, A. Hamo and S. Ilani, Realization of pristine and locally tunable one-dimensional electron systems in carbon nanotubes, *Nat. Nanotech.* **8**, 569–574 (2013).
- [31] A. Benyamini, A. Hamo, S. Viola Kusminskiy, F. von Oppen and S. Ilani, Real-space tailoring of the electron-phonon coupling in ultraclean nanotube mechanical resonators, *Nat. Phys.* **10**, 151–156 (2014).
- [32] F. Vigneau, J. Monsel, J. Tabanera, K. Aggarwal, L. Bresque, F. Fedele, F. Cerisola, G.A.D. Briggs, J. Anders, J.M.R. Parrondo, A. Auffèves, and N. Ares, Ultra-strong coupling between electron tunneling and mechanical motion, *Phys. Rev. Res.* **4**, 043168 (2022). <https://doi.org/10.1103/PhysRevResearch.4.043168>
- [33] C. Samanta, S. L. De Bonis, C. B. Møller, R. Tormo-Queralt, W. Yang, C. Urgell, B. Stamenic, B. Thibeault, Y. Jin, D. A. Czapslewski, F. Pistolesi & A. Bachtold. Nonlinear nanomechanical resonators approaching the quantum ground state, *Nat. Phys.* **19**, 1340–1344 (2023). <https://doi.org/10.1038/s41567-023-02065-9>
- [34] A. Palyi, P.R. Struck, M. Rudner, K. Flensberg, and G. Burkard, Spin-Orbit-Induced Strong Coupling of a Single Spin to a Nanomechanical Resonator, *Phys. Rev. Lett.* **108**, 206811 (2012). <https://doi.org/10.1103/PhysRevLett.108.206811>
- [35] A. Pfund, I. Shorubalko, K. Ensslin, and R. Leturcq, Suppression of Spin Relaxation in an InAs Nanowire Double Quantum Dot, *Phys. Rev. Lett.* **99**, 036801 (2007). <https://doi.org/10.1103/PhysRevLett.99.036801>
- [36] J. Danon, Y.V. Nazarov, Pauli spin blockade in the presence of strong spin-orbit coupling, *Phys. Rev. B* **80**,

- 041301 (2009). <https://doi.org/10.1103/PhysRevB.80.041301>
- [37] S. Nadj-Perge, S. M. Frolov, J. W. W. van Tilburg, J. Danon, Yu. V. Nazarov, R. Algra, E. P. A. M. Bakkers, and L. P. Kouwenhoven, Disentangling the effects of spin-orbit and hyperfine interactions on spin blockade, *Phys. Rev. B* **81**, 201305(R) (2010). <https://doi.org/10.1103/PhysRevB.81.201305>
- [38] R. Li, F.E. Hudson, A.S. Dzurak, A.R. Hamilton, Pauli Spin Blockade of Heavy Holes in a Silicon Double Quantum Dot, *Nano Lett.* **15**, 7314 (2015). <https://doi.org/10.1021/acs.nanolett.5b02561>
- [39] E.A. Laird, F. Pei, L.P. Kouwenhoven, A valley–spin qubit in a carbon nanotube, *Nature Nanotech.* **8**, 565 (2013). <https://doi.org/10.1038/nnano.2013.140>
- [40] E.A. Laird, C. Barthel, E.I. Rashba, C.M. Marcus, M.P. Hanson, and A.C. Gossard, Hyperfine-Mediated Gate-Driven Electron Spin Resonance, *Phys. Rev. Lett.* **99**, 246601 (2007). <https://doi.org/10.1103/PhysRevLett.99.246601>
- [41] F.C. Binder, S. Vinjanampathy, K. Modi, and J. Goold, Quantacell: powerful charging of quantum batteries, *New. J. Phys.* **17** 075015 (2015). <https://doi.org/10.1088/1367-2630/17/7/075015>
- [42] M. Perarnau-Llobet, K. V. Hovhannisyan, M. Huber, P. Skrzypczyk, N. Brunner, and A. Acin, Extractable Work from Correlations, *Phys. Rev. X* **5** 041011 (2015). <https://doi.org/10.1103/PhysRevX.5.041011>
- [43] O. Culhane, M.T. Mitchison, J. Goold, Extractable work in quantum electromechanics, *Phys. Rev. E* **106**, L032104 (2022). <https://doi.org/10.1103/PhysRevE.106.L032104>
- [44] N. Cottet, S. Jezouin, L. Bretheau, P. Campagne-Ibarcq, Q. Ficheux, J. Anders, A. Auffèves, R. Azouit, P. Rouchon, B. Huard, Observing a quantum Maxwell demon at work, *PNAS* **114**, 7561 (2017). <https://doi.org/10.1073/pnas.1704827114>
- [45] M. Josefsson, A. Svilans, A.M. Burke, E.A. Hoffmann, S. Fahlvik, C. Thelander, M. Leijnse, and H. Linke, A quantum-dot heat engine operating close to the thermodynamic efficiency limits, *Nature Nanotech.* **13**, 920 (2018). <https://doi.org/10.1038/s41565-018-0200-5>
- [46] T. Cubaynes, M.R. Delbecq, M.C. Dartiailh, R. Assouly, M.M. Desjardins, L.C. Contamin, L.E. Bruhat, Z. Leghtas, F. Mallet, A. Cottet, T. Kontos, Highly coherent spin states in carbon nanotubes coupled to cavity photons, *npj Quantum Information* **5**, 47 (2019). <https://doi.org/10.1038/s41534-019-0169-4>
- [47] P. Kammerlander, and J. Anders, Coherence and measurement in quantum thermodynamics, *Sci. Rep.* **6**, 22174 (2016). <https://doi.org/10.1038/srep22174>
- [48] M. Bild, M. Fadel, Y. Yang, U. von Lüpkke, P. Martin, A. Bruno, and C. Yiwon, Schrödinger cat states of a 16-microgram mechanical oscillator, *Science* **380**, 274 (2023). <https://doi.org/10.1126/science.adf7553>
- [49] P. Stadler, W. Belzig, and G. Rastelli, Ground-state cooling of a carbon nanomechanical resonator by spin-polarized current, *Phys. Rev. Lett.* **113**, 047201 (2014). <https://doi.org/10.1103/PhysRevLett.113.047201>
- [50] M. Forsch, R. Stockill, A. Wallucks, I. Marinković, C. Gärtner, R. A. Norte, F. van Otten, A. Fiore, K. Srinivasan, and S. Gröblacher, Microwave-to-optics conversion using a mechanical oscillator in its quantum ground state, *Nature Physics* **16** 69 (2020). <https://doi.org/10.1038/s41567-019-0673-7>
- [51] E.A. Laird, F. Kuemmeth, G.A. Steele, K. Grove-Rasmussen, J. Nygard, K. Flensberg, and L.P. Kouwenhoven, Quantum transport in carbon nanotubes, *Rev. Mod. Phys.* **87**, 703 (2015). <https://doi.org/10.1103/RevModPhys.87.703>
- [52] G.A. Steele, A.K. Hüttel, B. Witkamp, M. Poot, H.B. Meerwaldt, L.P. Kouwenhoven, and H.S. van der Zant, Strong coupling between single-electron tunneling and nanomechanical motion, *Science* **325** 5944, (2009). <https://doi.org/10.1126/science.1176076>
- [53] A. Castellanos-Gomez, H.B. Meerwaldt, W.J. Venstra, H.S. J. van der Zant, and A.G. Steele, Strong and tunable mode coupling in carbon nanotube resonators, *Phys. Rev. B* **86** 041402 (2012). <https://doi.org/10.1103/PhysRevB.86.041402>
- [54] F. Pistolesi, A.N. Cleland, and A. Bachtold, Proposal for a Nanomechanical Qubit, *Phys. Rev. X* **11** 031027 (2021). <https://doi.org/10.1103/PhysRevX.11.031027>
- [55] N. Ares, V.N. Golovach, G. Katsaros, M. Stoffel, F. Fournel, L.I. Glazman, O.G. Schmidt, and S. De Franceschi, Nature of Tunable Hole g Factors in Quantum Dots, *Phys. Rev. Lett.* **110** 046602 (2013). <https://doi.org/10.1103/PhysRevLett.110.046602>
- [56] D. Jirovec, P.M. Mutter, A. Hofmann, A. Crippa, M. Rychetsky, D.L. Craig, J. Kukucka, F. Martins, A. Ballabio, N. Ares, D. Chrastina, G. Isella, G. Burkard, and G. Katsaros, Dynamics of Hole Singlet-Triplet Qubits with Large g -Factor Differences, *Phys. Rev. Lett.* **128** 126803 (2022). <https://doi.org/10.1103/PhysRevLett.128.126803>
- [57] V.P. Michal, J.C. Abadillo-Uriel, S. Zihlmann, R. Maurand, Y.-M. Niquet, and M. Filippone, Tunable hole spin-photon interaction based on g -matrix modulation, *Phys. Rev. B* **107** L041303 (2023). <https://doi.org/10.1103/PhysRevB.107.L041303>
- [58] A. Crippa, R. Maurand, L. Bourdet, D. Kotekar-Patil, A. Amissé, X. Jehl, M. Sanquer, R. Laviéville, H. Bohuslavskyi, L. Hutin, S. Barraud, M. Vinet, Y.-M. Niquet, and S. De Franceschi, Electrical Spin Driving by g -Matrix Modulation in Spin-Orbit Qubits, *Phys. Rev. Lett.* **120** 137702 (2018). <https://doi.org/10.1103/PhysRevLett.120.137702>
- [59] K. Flensberg, and C.M. Marcus, Bends in nanotubes allow electric spin control and coupling, *Phys. Rev. B* **81**, 195418 (2010). <https://doi.org/10.1103/PhysRevB.81.195418>
- [60] A. Sen, G. Frank, B. Kolok, J. Danon, A. Pályi Classification and magic magnetic field directions for spin-orbit-coupled double quantum dots, *Phys. Rev. B* **108**, 245406, (2023). <https://doi.org/10.1103/PhysRevB.108.245406>
- [61] T. Pei, A. Palyi, M. Mergenthaler, N. Ares, A. Mavalankar, J. H. Warner, G.A.D. Briggs, and E.A. Laird, Hyperfine and Spin-Orbit Coupling Effects on Decay of Spin-Valley States in a Carbon Nanotube, *Phys. Rev. Lett.* **118**, 177701 (2017). <https://doi.org/10.1103/PhysRevLett.118.177701>